Somitic positional information guides self-organized patterning of snake scales

Tzika, Athanasia; Ullate Agote, Asier; Zakany, Szabolcs; Kummrow, Maya; Milinkovitch, Michel C.

How to cite

TZIKA, Athanasia et al. Somitic positional information guides self-organized patterning of snake scales. In: Science advances, 2023, vol. 9, n° 24, p. eadf8834. doi: 10.1126/sciadv.adf8834

This publication URL: https://archive-ouverte.unige.ch/unige:176387
Publication DOI: 10.1126/sciadv.adf8834

DEVELOPMENTAL BIOLOGY

Somitic positional information guides self-organized patterning of snake scales

Athanasia C. Tzika[1,2,3]*, Asier Ullate-Agote[1]†, Szabolcs Zakany[1], Maya Kummrow[4], Michel C. Milinkovitch[1,2,3]

Two influential concepts in tissue patterning are Wolpert's positional information and Turing's self-organized reaction–diffusion (RD). The latter establishes the patterning of hair and feathers. Here, our morphological, genetic, and functional—by CRISPR-Cas9–mediated gene disruption—characterization of wild-type versus "scaleless" snakes reveals that the near-perfect hexagonal pattern of snake scales is established through interactions between RD in the skin and somitic positional information. First, we show that ventral scale development is guided by hypaxial somites and, second, that ventral scales and epaxial somites guide the sequential RD patterning of the dorsolateral scales. The RD intrinsic length scale evolved to match somite periodicity, ensuring the alignment of ribs and scales, both of which play a critical role in snake locomotion.

INTRODUCTION

The two major chemical patterning processes in development are Turing's "reaction–diffusion" (RD) systems and Wolpert's "positional information," also known as the "French flag model" (*1*). The patterning of skin appendages, such as hairs, feathers, and scales, is dominated by the former process. For example, in mice, an RD model describes the emergence of primary hair placodes on the skin (*2*), whereas an expansion–induction model predicts secondary space-filling patterns by other types of hair follicles on the growing embryo (*3*). This micropatterning of hair placodes is superposed to the dorsoventral positional identity of the dermis, resulting in hair of different lengths and colors dorsally and ventrally (*4*). In flying birds, a spreading wave of ectodysplasin A (EDA) sets the threshold of mesenchymal cell density necessary to form a placode, resulting in the sequential addition of placode rows within the dorsal feather tracts (*5*). This process ensures the development of a regular pattern of feathers that has subsequently been lost in flightless species (*5*).

Snakes exhibit a strikingly ordered pattern of skin appendages: The dorsum and flanks are entirely covered by a highly regular hexagonal lattice of scales, whereas the ventrum is covered by a single column of large regularly spaced scales. The developmental dynamics establishing this near perfectly ordered pattern are unknown. Here, we morphologically, genetically, developmentally, and functionally—by CRISPR-Cas9–mediated gene disruption and the production of gene-edited snakes—characterize the so-called "scaleless" corn snakes. Whereas they lack dorsal and lateral scales, scaleless snakes exhibit nearly normal ventral scales, hinting at a different developmental mechanism for these two types of scales. Our genetic characterization of the scaleless mutant, together with the comparison of scaleless and scaled snake embryonic development, identifies that (i) ventral scales form independently of a functional canonical EDA pathway and their patterning is not self-organized but defined by positional information originating from underlying somitic tissues, (ii) the position of ventral scales guides a wave of self-organized patterning of the lateral scales, and (iii) a second wave of development appears near the dorsal midline and travels both ventrally (forming the dorsolateral scales) and dorsally (forming the most dorsal scales over the midline). Rare defects in the otherwise perfectly hexagonal lattice of skin scales form where the two lateral waves meet and are introduced because of geometrical constraints. Our numerical simulations, implementing a mechanochemical model of placode formation validated in chicken, show that both initial somitic positional information and traveling waves of self-organized placode development are required to recapitulate the observed snake morphogenetic dynamics and the final low count of defects in the snake skin-scale lattice.

RESULTS

The morphology of scaleless corn snakes

The corn snake (*Pantherophis guttatus*; Fig. 1A) is a species amenable to research due to the ease of its maintenance and breeding in a laboratory setting and the availability of numerous spontaneously occurring morphs affecting its coloration and skin appendages (*6*–*10*). Scaleless corn snakes (Fig. 1B and fig. S1, A and B), originating from the hybridization of a corn snake and a Great Plains rat snake (*Pantherophis emoryi*), were first reported in 2002 by a private breeder. These animals lack dorsal and lateral scales, whereas the transversely elongated ventral scales are present, although they are always split in two (right and left) or more parts. Small, isolated dorsolateral scales are occasionally present, mostly at the level of the cloaca and on the tail (fig. S1B). The number and position of these abnormal scales varies among individuals and is sex independent. On the head, only deformed labial, nasal, and prefrontal scales are present (Fig. 1B and fig. S1A). The absence of periocular scales makes the eyes look bigger. The same scale phenotype is observed in scaleless mutants of other species, such as the diamondback rattlesnake (*11*), the gopher snake (*12*), and the common water snake

[1]Laboratory of Artificial & Natural Evolution (LANE), Department of Genetics & Evolution, University of Geneva, CH-1211 Geneva, Switzerland. [2]SIB Swiss Institute of Bioinformatics, Geneva, Switzerland. [3]Institute of Genetics and Genomics of Geneva (iGE3), University of Geneva, Geneva, Switzerland. [4]Tierspital, University of Zurich, Zurich, Switzerland.
*Corresponding author. Email: athanasia.tzika@unige.ch
†Present address: Regenerative Medicine and Hemato-Oncology Programs, CIMA Universidad de Navarra; Instituto de Investigación Sanitaria de Navarra (IdiSNA), Pamplona, Spain.

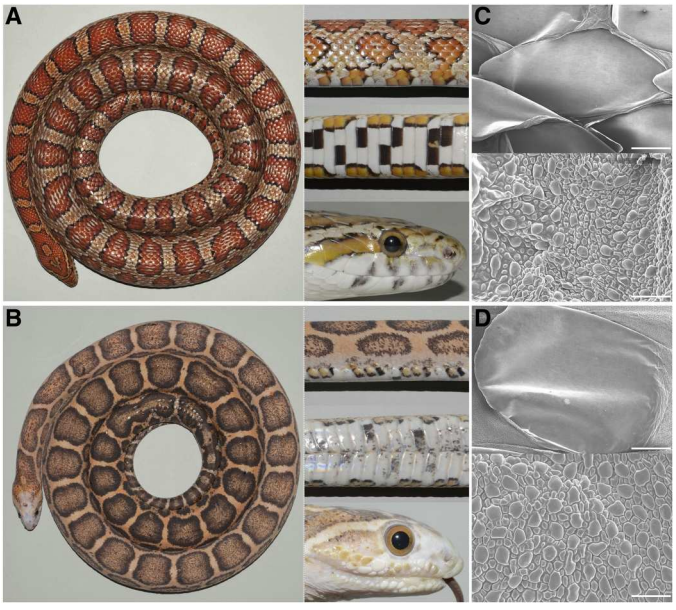

Fig. 1. Scaled and scaleless corn snakes. (**A** and **B**) Scale distribution in a scaled (A) and a scaleless (B) adult corn snake. A dorsal view (left) and close-ups of lateral, ventral, and head views (right) are shown. Adult corn snakes measure approximately 1.2 m. (**C** and **D**) Micrographs of dorsal scales (top; scale bars, 500 μm) and interscale skin (bottom; scale bars, 50 μm) of a scaled (C) and a scaleless (D) animal.

(*13*). Scaleless corn snakes shed their skin normally and grow well in captivity (fig. S1, C and D). Contrary to what was observed in the scaleless bearded lizards (*Pogona vitticeps*) (*14*), computerized tomography (CT) scans did not reveal evident differences in teeth morphology between the scaled and scaleless corn snakes (fig. S1E).

Scanning electron microscope imaging (Fig. 1, C and D) shows that the skin of scaleless individuals resembles the irregular surface of the interscale skin of scaled individuals, whereas the sparsely formed scales are less elongated than those of scaled animals. Histological sections (fig. S2) reveal that the papillary layer of the dermis with loose connective tissue is missing in the dorsal scaleless skin, similarly to the interscale regions of scaled animals, and it is greatly reduced in the rare dorsal scales present. The histological structure of ventral scales in scaleless animals is indistinguishable from that of scaled animals (fig. S2, B and D).

Genome mapping of the scaleless variant

Crosses in our captive-bred corn snake colony indicate that the scaleless phenotype is caused by a recessive single-locus variant. We crossed a scaleless female (*scl*/*scl*) and a heterozygous scaled male (+/*scl*) to obtain homozygous and heterozygous offspring for the scaleless locus. We sequenced whole-genome libraries of the two parental DNA samples and of two DNA pools from homozygous and heterozygous offspring with a coverage of 26.0× to 52.6× of the 1.7-Gb genome (table S1; Sequence Read Archive accession PRJNA953418). As previously described (*10*), we separately aligned each library to our corn snake genome assembly [National Center for Biotechnology Information (NCBI) accession GCA_001185365.2; (*10*)] and looked for nucleotide polymorphisms [single-nucleotide polymorphisms (SNPs) and multiple-nucleotide polymorphisms (MNPs)] co-segregating with the scaleless genotype in nonrepetitive regions. Based on our variant calling analyses, we identified a 4.3-Mb interval on Super-Scaffold_423 (NW_023010793.1; 37.3 to 41.6 Mb), harboring 11,101 co-segregating SNPs/MNPs with a density of 2.6 variants/kb (Fig. 2, A and B). MegaBLAST similarity searches showed synteny with chromosome 1 of *Anolis carolinensis* (216.1 to 221.9 Mb, version 2) and chromosome 3 of *Gallus gallus* (35.3 to 39.9 Mb, version 6). Forty-two protein-coding genes are present in the corn snake interval and in the syntenic region of the eastern brown snake (*Pseudonaja textilis*); 46 and 45 genes are present in the corresponding regions of the *A. carolinensis* and *G. gallus* genomes, respectively (table S2).

Most of the co-segregating variants in coding sequences in the interval correspond to amino acid substitutions (table S2). Multiples-of-three deletions were found in the coding sequence of three genes (*Opsin 3*, *Egl-9 Family Hypoxia Inducible Factor 1*, and *Exocyst Complex Component 8*); they result in the deletion of 1 or 2 amino acids and leave the protein structure unaffected, as supported by InterProScan analyses (*15*). Conversely, a 2-nucleotide (nt) deletion (TAC to T) was found within the coding sequence of the *ectodysplasin A receptor–associated adapter* gene (*EDARADD*) at position 39,572,202 of Super-Scaffold_423. The deletion occurs in exon 6 at position 182 of the 215–amino acid protein. It introduces a frameshift, resulting in a premature STOP codon at that exact place by changing the TGT triplet (cysteine) to TAA (STOP) and a protein shorter by 33 amino acids. InterProScan analyses reveal that the highly conserved DEATH domain, normally spanning amino acids 128 to 198, is thus truncated (Fig. 2C).

EDARADD is a key component of the EDA pathway: It works as an intracellular protein adapter to the transmembrane receptor EDAR, leading to downstream activation of the transcription factor Nuclear factor kappa-light-chain-enhancer of activated B cells (NF-κB) by means of the TAB2/TRAF6/TAK1 signaling complex (*16*). Because of the partial deletion of the DEATH domain in scaleless snakes, EDARADD is likely to lose its affinity to EDAR, cancelling the activation of the downstream NF-κB pathway. The EDA pathway plays a key role in the development of ectodermal appendages including hairs, feathers, scales, and teeth (*14*, *17*). Modifications of EDARADD in humans cause hypohidrotic ectodermal dysplasia (HED), a disorder characterized by deficient sweat glands, sparse hair, and missing teeth (*18*). In mice, even a single amino acid substitution near the DEATH domain results in the HED phenotype (*19*, *20*). In humans, a 2–amino acid deletion in the DEATH domain impairs the function of EDARADD and causes HED (*21*). The role of the EDA pathway is highly conserved throughout vertebrate evolution. Disruption of EDA, the ligand of EDAR, in bearded lizards results in scaleless animals, lacking most of their dorsal and ventral scales (*14*). Similarly, the scales and teeth of *eda* and *edar* mutant zebrafish and medaka fish, respectively, are impacted (*22*, *23*).

We confirmed the absence of the corn snake scaleless 2-nt deletion in genomic libraries of seven unrelated scaled (+/+) individuals (table S1). Furthermore, we sequenced the genomic region flanking the 2-nt deletion in the family members used for the mapping (table S3) and in 67 animals from 31 unrelated lineages (8 *scl*/*scl*, 2 +/*scl*, and 57 +/+; table S4). We found that the deletion is fully concordant with the scaleless phenotype, a result further confirmed by sequencing of *EDARADD* mRNA transcripts from wild-type and scaleless individuals.

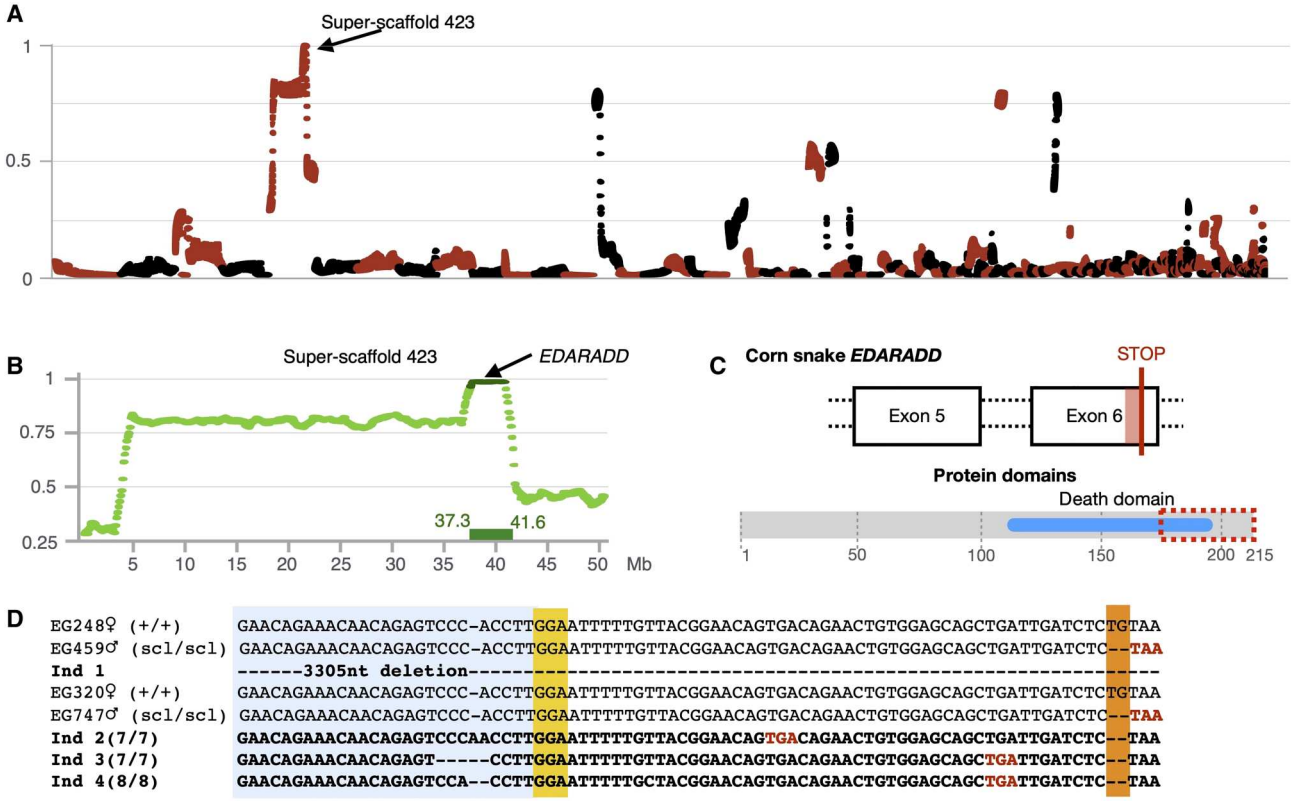

Fig. 2. Disruption of *EDARADD* results in the scaleless corn snake phenotype. (**A**) Proportion (*y* axis) of quality-filtered SNPs/MNPs co-segregating with the *scaleless* locus in the four genome libraries, compared to informative quality-filtered parental variants (homozygous in the *scl/scl* female and heterozygous in the *scl*/+ male). Scaffolds (alternatively colored black and red) are ordered from longest to shortest. The super-scaffold containing the *scaleless* interval is indicated. (**B**) Proportion (*y* axis) of quality-filtered SNPs/MNPs co-segregating with the *scaleless* locus on Super-scaffold 423. Dark green dots correspond to the 4.3-Mb region with the highest proportion of co-segregating variants. *EDARADD* is in this interval. In (A) and (B), proportions are calculated for scaffolds >1 Mb, with a 1-Mb sliding window and a step of 100 kb. (**C**) Impact of the 2-nt deletion (red shade on exon 6) on the structure of the *EDARADD* transcript (red line, STOP codon) and protein (red dashed rectangle, truncated part). The exons are not drawn in proportion. (**D**) Sequence information on the CRISPR-Cas9–induced *EDARADD* mutations. Parents and mutated offspring are indicated in plain and bold fonts, respectively. The ratio in parenthesis for individuals 2, 3, and 4 corresponds to the number of clones with this sequence. Blue shading, gRNA sequence; yellow shading, PAM sequence; orange shading, original scaleless 2-nt deletion; bases indicated in red form STOP codons.

CRISPR-Cas9 EDARADD disruption in snakes

CRISPR-Cas9 gene editing was recently used to produce knockout *Anolis* lizards by injecting pre-vitellogenic oocytes (*24*). We adapted this protocol to the seasonal breeding of corn snakes and the larger size of their oocytes to produce gene-edited snakes. First, we selected a guide RNA (gRNA) that successfully generates a knockout corn snake fibroblast cell line by targeting exon 6 of *EDARADD*. The PAM site of the selected gRNA is 50 base pairs (bp) upstream of the scaleless 2-nt deletion. We then injected a mixture of the Cas9 protein and the gRNA in pre-vitellogenic oocytes of five scaled females (+/+). In the ovaries, we found oocytes at variable stages of maturation, but only the pre-vitellogenic ones were injected. Three treated females were then crossed with scaleless males (*scl/scl*) and two with heterozygous males (+/*scl*). In total, we injected 96 oocytes; the females laid 69 eggs, 54 of which hatched to give four scaleless animals (fig. S3). These were produced by two of the three females crossed with a scaleless male. The remaining 50 hatchlings were all scaled.

We extracted DNA from hatchling sheds and sequenced exon 6 of *EDARADD*. All scaled individuals were either +/+ or +/*scl* depending on the genotype of their sire (table S5). Sequencing of the scaleless animal DNA (Fig. 2D) showed that individual 1 carries a 3305-nt deletion spanning exon 6 and the flanking intronic regions, individual 2 has a 1-nt insertion that introduces a STOP codon 26 bp downstream, individual 3 has a 4-nt deletion that introduces a STOP codon 43 bp downstream, and individual 4 has a 1-nt deletion that introduces a STOP codon 45 bp downstream. All introduced mutations are in homozygosity and absent from the parental DNA. In addition, individuals 2, 3, and 4 are also homozygous for the scaleless 2-nt deletion, although we expected them to be heterozygous based on the genotype of the parents. It was previously reported that induced double-strand breaks (DSBs) in one parental allele of human embryos is predominantly repaired using the homologous gene from the other parent, favoring a homology-directed repair (*25*). We observe that a similar process occurred in the gene-edited corn snakes: The CRISPR-induced DSB in the maternal wild-type allele was repaired using the homologous scaleless paternal allele, and short indels were introduced at the break site. In all four transgenic snakes obtained here, disruption of exon 6 of *EDARADD* results in scaleless individuals whose skin phenotype is indistinguishable from the other (not gene-edited) scaleless animals in our colony. This unambiguously demonstrates that the

original scaleless phenotype is caused by the *EDARADD* mutation identified above by genome mapping. As DNA extractions were performed on skin sheds, we cannot evaluate the potential mosaicism of the gene-edited individuals, although cloning of the amplified exon 6 from sheds did not reveal the presence of alternative alleles. The heritability of the CRISPR-Cas9–induced mutations will be tested when the animals reach sexual maturity at the age of 4 years.

Disruption of placode signaling in scaleless snakes

Reptilian scales develop from placodes (*14*), i.e., local spots of epidermal thickening and dermal condensation that both act as a signaling center. The only known exception is the formation of scales on the face and jaws of crocodiles through a self-organized mechanical stress–induced folding of the skin (*26*). Previous studies have shown that placodes in amniotes express the activators of placode formation b-catenin (*CTNNB1*) and Sonic hedgehog (*SHH*) (*14*, *27*). We performed whole-mount in situ hybridization (WISH) of species-specific probes to understand the impact of the *EDARADD* mutation in scaleless snakes on the expression pattern of *CTNNB1* and *SHH* (Fig. 3, A and B). In scaled embryos, localized and placode-specific signal is visible starting at 14 days post-ovoposition (dpo) dorsally and ventrally. In scaleless embryos, expression is maintained only in the ventral scale precursors but is lost on the dorsal and lateral skin, although we could observe faint, diffuse, and transient *CTNNB1* expression at the dorsal side at 18 dpo (fig. S4A). This expression was near the cloaca where scales occasionally form in scaleless individuals. We also investigated the *fibroblast growth factor 20* (*FGF20*) expression because an *FGF20* mutation is responsible for a scaleless and featherless phenotype in chicken (*28*). In mice, it has been shown that Fgf20 acts downstream of the EDA and WNT pathways and initiates dermal condensation underneath the epidermal thickening of the placode (*29*). While we observe localized *FGF20* expression in all ventral and dorsolateral placodes in scaled embryos, we do not detect localized expression in scaleless animals, neither dorsally nor ventrally (Fig. 3C).

Regarding the expression of the EDA pathway members in scaled embryos (Fig. 3, D to F, left panels), the extracellular ligand *EDA* is strongly expressed in the interscale skin, similarly to its interfollicular expression in developing chicken embryos (*30*), whereas the expression of the transmembrane receptor *EDAR* is restricted to the developing scales. Furthermore, we identified strong expression of *TROY* within placodes at early stages of scale development (12 dpo), i.e., before any signal could be detected for the other markers discussed above. The receptor TROY has been associated with the formation of secondary hair in mammals (*31*, *32*), as well as feathers and scales in chicken (*33*). Note that WISH did not reveal localized expression of *XEDAR* or *EDARADD*, two other members of the EDA pathway, in scaled and scaleless embryos at the relevant stages of development (fig. S4, B and C). It is likely that the expression of these genes is too low to be detected by WISH, although it has been observed in the developing feather placodes in chicken (*30*, *33*).

Similar in situ hybridization experiments with scaleless embryos (Fig. 3, D to F, right panels) reveal that *EDARADD* mutants lack the dorsal expression of *EDAR* and exhibit strong but perturbed dorsal expression of *EDA* and *TROY*, i.e., the signal is highly irregular compared to that observed for *EDA* (at the lattice's edges) and *TROY* (within each future scale) in scaled embryos (variation of expression along the body is shown in fig. S5A). Our findings in scaleless snakes are reminiscent of those reported for scaleless chicken (*34*), where some EDA pathway genes are expressed but their spatial distribution is disrupted. The development of occasional dorsal scales seen on scaleless individuals might correspond to regions where local EDA and TROY signaling of sufficient strength randomly aligns within the disrupted patterns of expression (fig. S5, B to D). However, it is important to mention that the expression of *EDAR* is nondetectable dorsally in scaleless embryos, and the role of TROY in scale formation remains to be fully understood. Strikingly, the expression of the three markers (*EDA*, *EDAR*, and *TROY*) discussed above is equally strong (although occasionally fragmented) in the ventral scales of scaled and scaleless embryos (Fig. 3, D to F, right panels). Hence, as ventral scales in scaleless animals form normally and their regular spacing is not affected, our analyses indicate that a functional EDARADD is necessary for the development and proper spatial distribution of dorsal and lateral snake scales, but not of the ventral ones. This is a unique example of skin appendages forming properly in the absence of a functional canonical EDA pathway.

Ventral scale and somitic derivative correspondence

At early stages of corn snake development (0 to 10 dpo), we observe regularly spaced bulges along the entire length of the embryo. These bulges coincide first with somites and later with their dermomyotome derivatives (Fig. 4, A and B). The bulges persist ventrally as the ventrolateral lip (VLL) of the dermomyotome progresses to envelop the intraembryonic cavity. Remarkably, the expression of *TROY*, and then of other placode markers, is first observed on these ventral bulges (Fig. 4C, fig. S6A, and movie S1). In other words, ventral scales, in both scaled and scaleless embryos, form exactly on these VLL bulges. Our CT scan imaging reveals that the correspondence of ventral scales with somitic derivatives in corn snake embryos is translated in adult snakes by the exact matching between the number of ventral scales and distal ribs (Fig. 4D and fig. S6, B and C).

Among the 147 juvenile and adult snakes visually inspected, we found defects in the formation of ventral scales in 12 animals (table S6), i.e., we observed supernumerary ventral scales (e.g., red contours in Fig. 4, E to G) at the right and/or left side of the ventrum. Full-body CT scan imaging of two of these animals showed that they present two types of skeletal defects. In the first type, we observe an additional rib from the side where the supernumerary ventral scale appears (Fig. 4E). Note that, during snake development, the coelum is open and the two halves of the ventral scales independently form on either side of this opening. The left and right halves then merge when the coelum gradually closes in a cephalocaudal direction. However, this merging is not a discrete iterative process, where a ventral scale has to fully merge before the next one initiates its merge. Fusion rather occurs simultaneously for several consecutive scales (fig. S6D). Depending on how the right and left parts of the ventral scales are aligned when they merge, the supernumerary scale and rib do not always superpose, but appear in proximity. In other words, the supernumerary somitic structure (rib) generates a supernumerary half-ventral scale that, in turn, causes a slippage in the alignment of left and right halves of ventral scales. The defect corresponding to the lack of correspondence between the number of left and right halves of ventral scales

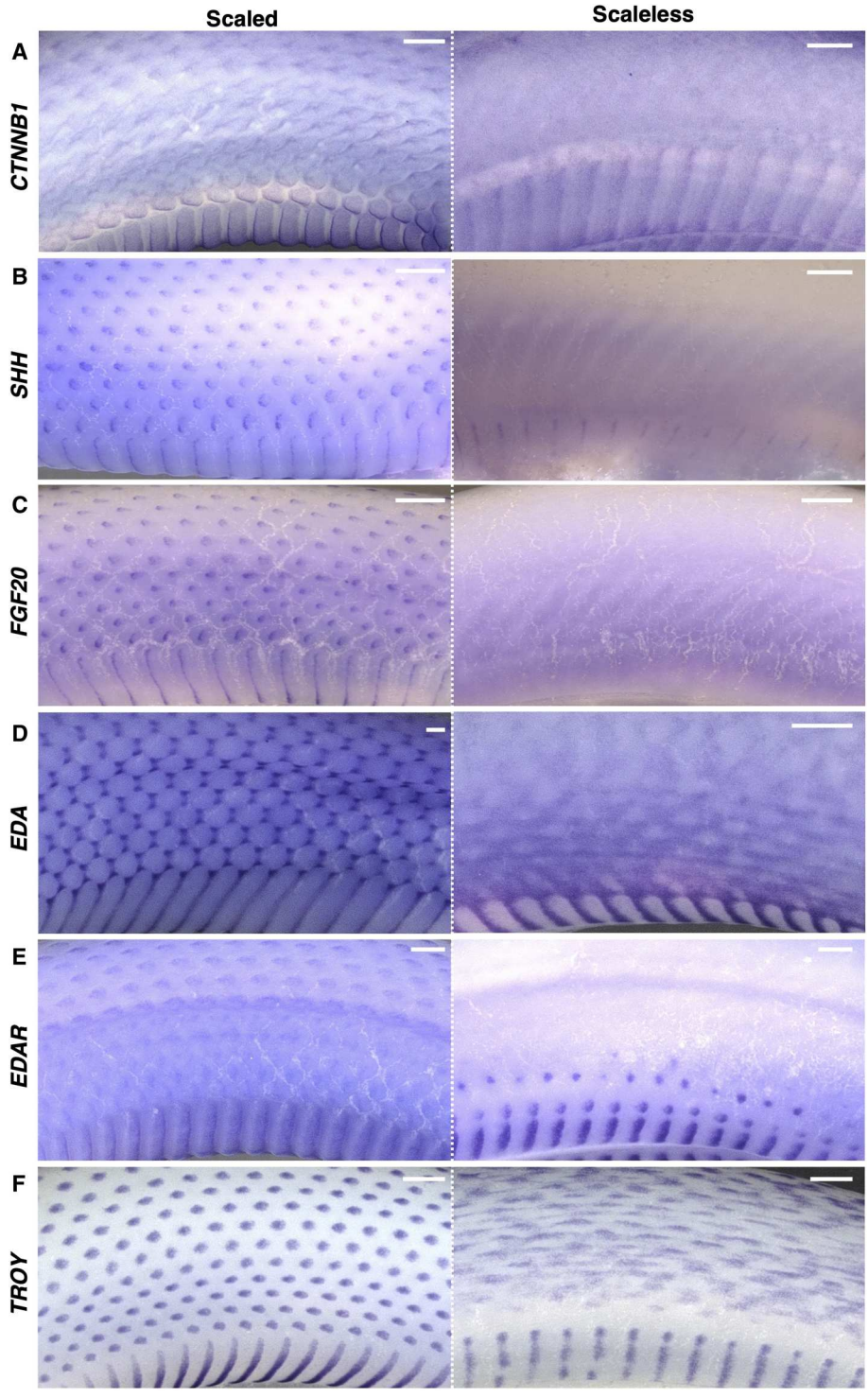

Fig. 3. Spatial distribution of placode markers in scaled and scaleless corn snakes. WISH of species-specific probes for (**A**) *CTNNB1*, (**B**) *SHH*, (**C**) *FGF20*, (**D**) *EDA*, (**E**) *EDAR*, and (**F**) *TROY* on scaled and scaleless embryos collected at days 18 to 22 po. Scale bars, 500 μm.

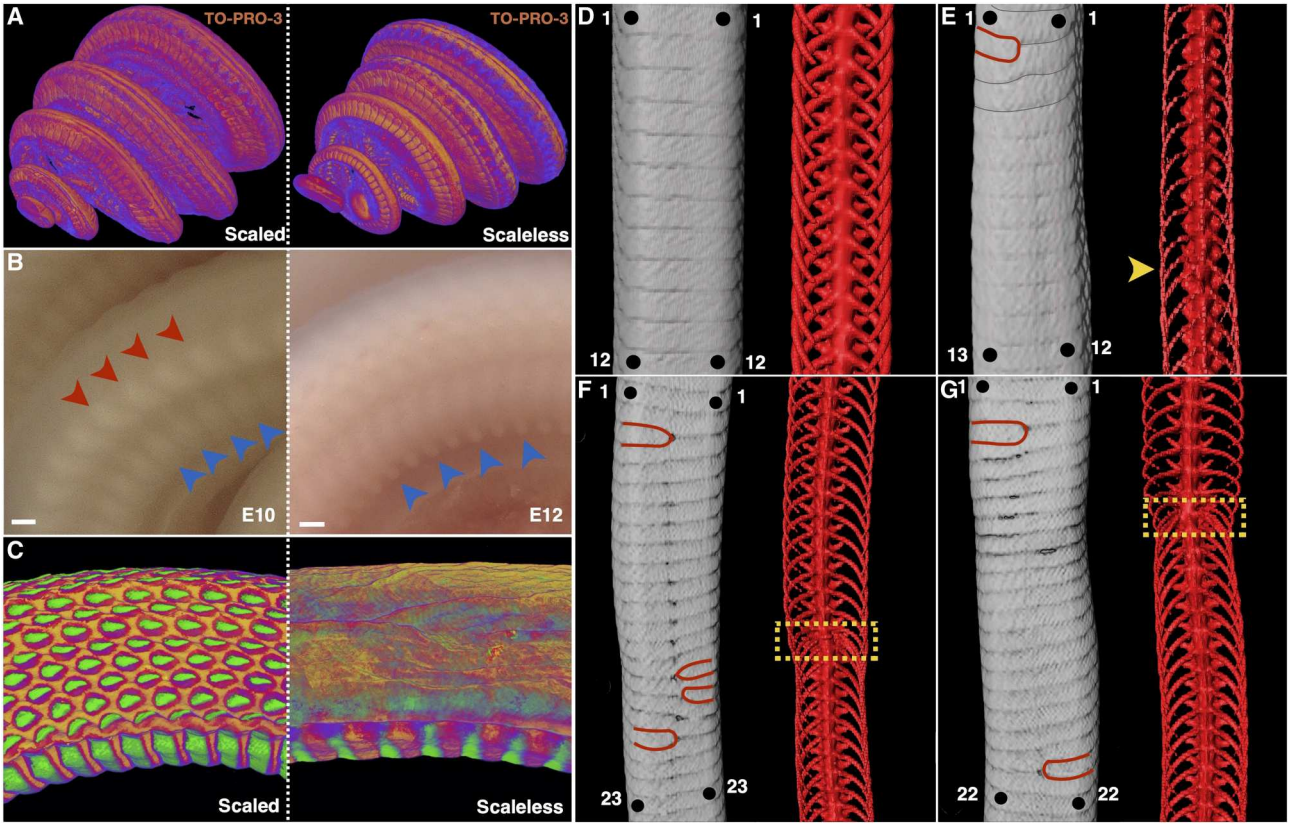

Fig. 4. Correspondence between somitic structures and ventral scales. (**A**) TO-PRO-3 nuclear staining of a scaled and a scaleless embryo at day 3 po highlighting the somitic structures. (**B**) Unstained scaled embryos at days 10 and 12 po with evident bulges (red arrowheads, epaxial; blue arrowheads, hypaxial). Scale bars, 200 μm. (**C**) Double fluorescent WISH of *EDA* (red) and *TROY* (green) hybridization chain reaction probes on a scaled and a scaleless embryo at day 16 po. (**D** to **G**) Surface reconstructions (gray) and segmented bones (red) of adult scaled (+/+) snakes: (D) Individual with no skeletal deformations. (E) Individual with a supernumerary scale (red contour) and a supernumerary rib (yellow arrowhead). (F and G) One snake with perturbed ventral scale patterning (red contours). In (F), the animal has two consecutive vertebrae (yellow rectangle) that each has four ribs instead of two. Thus, there are two supernumerary ribs at each side, which is also reflected in the number of ventral scales, i.e., two supernumerary scales at each side. In (G), the animal has one vertebra (yellow rectangle) with four ribs instead of two. Thus, there is one supernumerary rib at each side, which is also reflected in the number of ventral scales, i.e., one supernumerary scale at each side. Numbers correspond to the number of ventral scales on the right and left side of the animals.

appears in the vicinity, but not exactly at the position, of the supernumerary rib. In the second type of skeletal defects, two left and two right ribs (instead of one of each) form on the same vertebra (Fig. 4, F and G, yellow dashed rectangles, and fig. S6E). In this case, the number of ribs and scales is the same on each side but the alignment of the right and left part of the ventral scales is impacted near the supernumerary ribs. It is also important to stress that the somitic structures that influence the positioning of the ventral scales form at an early stage (before E10), whereas the merging process starts later in development (E20 and onward). The shape and size of the embryo change during this interval, and the tight coils of early-stage embryos as seen in Fig. 4A relax (fig. S5A).

We also performed CT scans on two other snakes species: the red bamboo snake (*Oreocryptophis porphyraceus*) and the ball python (*Python regius*) (fig. S7, A and B). These species (i) have different body morphologies than the corn snake—one with a slenderer body and the other more heavily built, (ii) belong to different snake lineages that separated from corn snakes 15 and 86 million years ago, respectively, and (iii) have ventral scales of different sizes (width) along the body axis (corn snake: ~54 mm, red bamboo snake: ~48 mm, ball python: ~63 mm; fig. S7C). Despite these interspecific differences, the number and position of ventral scales match those of the underlying ribs, showing that this is a common feature of different snake lineages. Our findings suggest that the presence of a well-developed VLL in proximity to the ventral skin induces the ventral scale placode formation through a yet undefined mechanical or signaling mechanism, or a combination of both. Note that, as a result of this alignment between VLL bulges and ventral scales, each ventral scale is associated to individual muscles (Fig. 5A).

How the dorsolateral scales get ordered

During snake embryogenesis, somites are progressively added caudally, while the anterior part of the body continues to further develop. Thus, an embryo at any stage of development recapitulates a time series of developmental stages with the anterior part being more advanced than the posterior. Scale development occurs after the completion of somitogenesis, between 14 and 30 dpo. WISH targeting *TROY* expression, the earliest detectable placode marker, reveals that a first line of lateral placodes develops ventrally (panel a

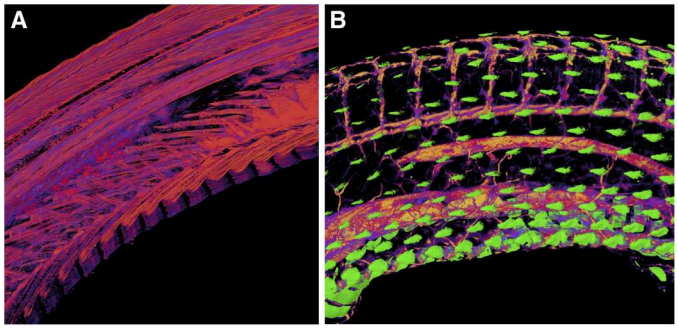

Fig. 5. Correspondence of scales to somitic structures. (**A**) Scaled embryo at 18 dpo immunostained with an antibody targeting *Myosin*. Each ventral scale is associated to individual muscles. (**B**) Double fluorescent WISH of *EDA* (red) and *TROY* (green) hybridization chain reaction probes on a scaled embryo at day 16 po. In this case, we only show the background signal in the channel of the *EDA* probe detection. Dorsally, we observe regularly spaced autofluorescent structures (red), which are probably the vessels corresponding to each somite. Their spacing corresponds to the spacing of the scales as highlighted by the *TROY* probe (green).

in Fig. 6A, row 1), and these placodes are positioned in anti-phase with the ventral scales. Then, additional lines of placodes successively appear, and the placodes are positioned in anti-phase with the placodes of the line below (panels b to d; rows 2 to 6). At the same time, a second wave of expression appears near the dorsal midline, and travels ventrally, forming successive lines of expression that similarly split into placodes (panels c and d; rows 7 to 10). This wave is probably also aligned to somitic structures, as we observe that the spacing of the dorsal placodes corresponds to the spacing of other structures of somitic origin (Fig. 5B). The two traveling waves of placode formation eventually meet laterally. The final number of formed scale lines depends on the local diameter of the embryo. As the neural tube closes, the skin over the dorsal midline thickens (fig. S8). This allows for a third wave of placode formation to initiate and progress dorsally over the new skin; the waves of the left and right sides of the embryo eventually meet at the dorsal midline (Fig. 7A). The combination of these three waves (Fig. 6B) results in the highly ordered hexagonal lattice of dorsolateral scales.

Our inspection of 147 corn snakes confirms that defects in the otherwise perfect hexagonal pattern of dorsolateral scales are rare and located where the two waves meet laterally. Fundamental geometrical constraints lead to the introduction of defects as the animal's diameter reduces. Conversely to a cylinder, the side of a cone cannot, in general, be paved by a strictly hexagonal lattice, except for the six cones corresponding to the six inequivalent rotations, which are symmetries of the lattice. It can easily be shown that the corresponding half-apertures of the six exception cones are $\arcsin(n/6)$, where n = 1,2, ...,6 (fig. S9). The exception cone with the smallest aperture [$\arcsin(1/6) \approx 0.1674$] is still much too large to approximate any part of the body of a snake embryo. Hence, the snake body cannot be paved by a hexagonal lattice without defects.

To quantify our observations, we reconstructed the three-dimensional (3D) surface micro-geometry of three corn snakes using an in-house imaging robotic system and software pipeline (*35*). The scale neighborhood was obtained by constructing local 2D Delaunay triangulations of projected polygonal patches representing scale boundaries (local projections of 3D positions in normal planes of patches) (Supplementary Text; fig. S10). The number of topological defects, i.e., departure from hexagonal connectivity, is very low (0.6%), with an average of 33 scales out of 5132, and they all appear on the flanks (mean angular distribution from the dorsal midline = 51° to 69°), where the dorsal and ventral waves of placode development meet (Fig. 8, A to C, and fig. S11). The defects correspond to scales with five and seven nearest neighbors that always appear as a pair where two cephalo-caudal lines of scales split to become two or merge to become one, as we can also observe in embryos (Fig. 7B). These defects are located at corresponding regions along the body of the three imaged animals and often symmetrically on the right and left sides (Supplementary Text; fig. S12). In addition, we measured the size of the lateral side of an embryo along its length (fig. S13) and found that it increases in the area of the externalized heart and liver, roughly corresponding to the ventral scales 50 to 100, before to decrease again more caudally. Our analyses of the adult dorsolateral scales show that the number of lines also increases up to the corresponding region (ventral scales 50 to 100; red rectangles in Fig. 8, A and C, and fig. S11, A, C, D, and F) and then the number of lines decreases. Thus, the position of dorsolateral defects along the body of the animals is very likely related to the embryonic body morphology when the scale patterning forms. Note that a much greater number of defects is found near the head and cloaca, areas where the body morphology transitions from head to body and body to tail, respectively.

Prepositioned traveling waves in snakes

In chicken, a reaction–diffusion–taxis system has been proposed to explain how the *EDA* signaling wave that sweeps across the skin controls the density of mesenchymal cells necessary to form a hexagonal pattern of feathers (*5*). We adapted the mathematical model describing this process (*36*) to the context of snake scale development (fig. S14). Simulations performed on a planar domain resembling the conical shape of the snake body in the absence of traveling waves generate a lattice of placodes with a very large proportion of defects (54%; Fig. 8D). When two opposing waves (ventral and dorsal) of placode development are introduced, the pattern becomes more ordered, but the proportion of defects (19%) remains higher than in real snakes and the defects are spread all over the domain (Fig. 8E). When the interplacodal distance is fixed in the initial row for the lower wave (=prepatterned wave), mimicking the positional information brought about by the somite–guided ventral scales in real snakes, the pattern order increases in the lower half of the domain and the defects exclusively appear in the upper half as well as where the two waves meet (Fig. 8F). Finally, when both waves are prepatterned, the simulations reproduce topologically and statistically our findings on the real snakes (Fig. 8G): An ordered hexagonal pattern is produced with pairs of defects (five and seven nearest neighbors) located where two cephalo-caudal rows of scales merge into one. The positional information conveyed from the ventral scales is necessary to establish the near-perfect hexagonal lattice of the dorsal scales. This is illustrated in the animal exhibiting a single supernumerary ventral scale from one side (Fig. 4E): The extra ventral scale causes the development of a supplementary scale in each row of dorsolateral scales. As these supernumerary scales must be accommodated, the alignment of the left and right side dorsolateral scales is affected, resulting in a defect along the dorsal midline (fig. S15). This

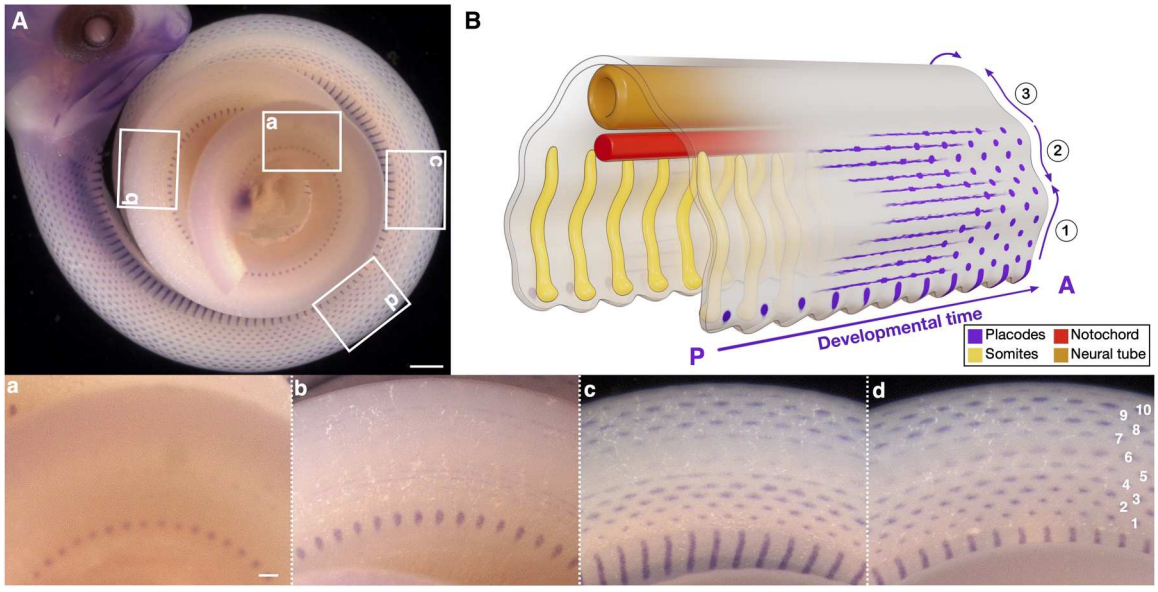

Fig. 6. Dorsal scale patterning in corn snakes. (**A**) WISH of a *TROY* probe on an embryo at day 16 po. Panels (a) to (d) correspond to the marked regions on the entire embryo. The scale row numbers are shown in (d). Scale bars, 1 mm (main) and 200 μm (insets). (**B**) Schematic representation of the scale patterning process. Initially, expression of placode-specific markers appears ventrally over the VLL of the dermomyotome. Then, three traveling waves of EDA signaling induce the development of the lateral and dorsal scales: 1, starts just above the ventral scales and travels upward; 2, starts dorsolaterally and travels downward; and 3, starts at the same position as wave 2 but travels upward to join the traveling wave from the other side of the embryo. A, anterior; P, posterior.

example illustrates again that defects tend to appear close to, but not exactly at the position of, their proximal cause: (i) A supernumerary ventral half-scale appears close to, but not at, the position of supernumerary ribs, and (ii) lattice defects appear close to, but not at, the position of supernumerary ventral half-scale. Regarding point (ii), as the RD system can tolerate for the scales to be somewhat "pushed around," defects do not appear in the dorsolateral lattice of scales when left and right supernumerary ventral scales appear close enough to each other along the animal.

To test how close the interplacodal distance in the initial ventral and laterodorsal rows must be to the intrinsic length scale $L \approx 3.2$ (in arbitrary units) of the self-organized patterning system (i.e., the mean distance among direct neighbors), we performed simulations varying the former. On a planar projection of a cone, the number of defects is very small when the interplacodal distance in the initial row is set to $L = 3$, whereas numerous defects are introduced across the domain when this distance is decreased or increased by 1/3 (fig. S16). Furthermore, simulations with two prepatterned waves on a 3D geometry approximating the adult snake-like body shape (Fig. 8, H to J) generate defects with spatial distribution and topological features that match those observed on the real animals. Hence, all our simulations show that both the ventral and dorsal waves need to be initially prepatterned with the same typical length scale for the near-perfect hexagonal lattice to form. Note that our numerical simulations based on a simpler canonical activator-inhibitor RD model (*37*, *38*) previously used in the context of placode formation (*39*, *40*) (Supplementary Text; fig. S17) generate similar results, indicating that the mechanism we propose here (prepattern of ventral scales combined with two waves of self-organized placode development) is robust to model variation. Whereas our analyses identify that the ventral scales, positioned by the underlying VLL somitic bulges, set the positioning of the first ventral row of lateral scales in anti-phase with the ventral scales, the structures—possibly of somitic origin (Fig. 5B)—that guide the initial row of the dorsal wave remain to be identified.

DISCUSSION

Our genomic mapping and functional analyses, together with the production of genetically modified snakes, demonstrate that the disruption of *EDARADD* is responsible for the scaleless corn snake phenotype. We thus show that functional EDA, EDAR, and EDARADD interactions are necessary for the highly ordered formation of dorsal and lateral scales, but not of the ventral ones. This result is coherent with our in situ hybridization experiments showing that the spatially ordered expression of EDA pathway genes and other placode markers is disrupted in the developing dorsolateral scaleless skin, but maintained ventrally. Furthermore, no *FGF20* expression could be detected neither dorsally nor ventrally in scaleless embryos. In mice and chicken, EDA signaling activates the production of *FGF20*, which in its turn induces the formation of a dermal condensate (*5*, *29*). Hence, our observations indicate that ventral snake scales develop independently of FGF signaling. Our study suggests that dermal condensation, and the corresponding development of a ventral scale, is induced by another factor, either molecular or mechanical, associated to the underlying bulge formed by the hypaxial somite.

The expression of *TROY*, an alternative receptor in the EDA pathway, reveals that there are three traveling waves of placode formation on the lateral and dorsal snake skin (Fig. 6B). The first is anchored to the preexisting ventral scales and travels dorsally. The second, initiating laterodorsally and traveling ventrally, is possibly aligned to the epaxial part of the somites. The third wave initiates at the same location as the second wave, but it travels dorsally when

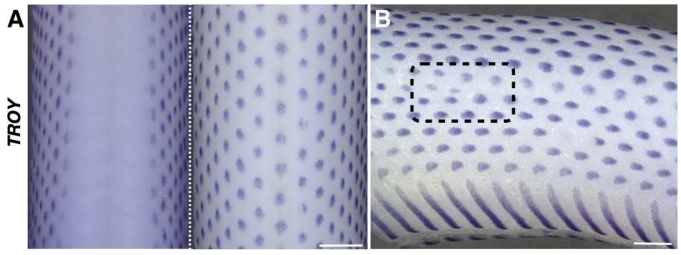

Fig. 7. Dorsal and lateral waves of placode formation. (**A**) Dorsal view of WISH of a *TROY* probe at 12 (left) and 18 (right) dpo to illustrate how the left and right traveling waves of placode formation join on the dorsal midline. (**B**) WISH of a *TROY* probe at 18 dpo: A defect is highlighted in the dashed rectangle, where two lines of placodes merge to form one. Scale bars, 500 μm.

the dorsal skin becomes thick enough, i.e., when the density of mesenchymal cells becomes dense enough for the self-organized patterning process to occur. Although this remains to be confirmed, we suggest that these waves propagate in a similar manner as in developing chicken embryos, where a traveling wave of EDA lowers the threshold of mesenchymal cell density required for a placode to form, and thus, rows of placodes are added in a sequential manner (*5*). Whatever is the exact molecular mechanism generating the waves of placode development, our analyses indicate that the development of dorsolateral scales in snakes is a self-organizational process and that the three waves are prepatterned by underlying somitic structures, allowing for the formation of the spectacular, nearly perfect, hexagonal lattice of scales. Note that the zebrafish scales are also organized in a hexagonal lattice and that the squamation patterning might correlate with the segmented musculature of the myotomes (*41*). The mechanistic link between myotomes and scale placode development remains unresolved, although the timing of events as regulated by the thyroid hormone seems to play an important role. Our study also gives credence to the suggestion that scutes of the tortoise shell develop in alignment with myosepta (*42*), contrary to modeling studies of the carapace scute formation favoring a hierarchically nested RD mechanism over the guidance of an underlying prepattern (*43*, *44*).

Remarkably, our analyses indicate that the intrinsic length scale of the self-organized patterning system of snake scales has been tuned during evolution to match the periodicity of the somites. This connection is particularly evident when considering the perfect correspondence between, on the one hand, the distance between neighboring scales on the flanks and, on the other hand, the distance between successive ventral scales, which, in turn, exactly corresponds to the distance between successive VLL somitic ventral bulges. We reason that this match ensures the reproducibility of the scale pattern among individuals and the alignment of muscles, ribs, and scales, all of which play key roles in snake locomotion (Fig. 5A) (*45*).

MATERIALS AND METHODS

Animals

Corn snakes were housed and bred at the Laboratory of Artificial & Natural Evolution (LANE) animal facility running under a veterinary cantonal permit. The individuals were sampled and imaged following Swiss law regulations and under experimentation permits GE24/33145 and GE201/19 approved by the Geneva cantonal authorities.

Histology, staining, and imaging

Gold-coated skin sheds were imaged using the scanning electron microscope JEOL JSM-6510LV. Dorsal and ventral skin was fixed in 4% paraformaldehyde and dehydrated in ethanol before embedding in paraffin blocks. Seven-micrometer microtome sections were deparaffinized, hematoxylin and eosin–stained, and imaged with a Pannoramic MIDI slide scanner. Micro-CT scans of adult heads were performed using a Quantum GX micro-CT scanner (PerkinElmer) at 90-kV acceleration voltage, 45-mm field of view (FOV), 90-μm voxel size, high resolution setting, and 4-min scans. Full-body CT scans were performed with a LightSpeed VCT 64 scanner in helical mode, a thickness of 0.625 mm, and a spacing of 0.312 mm.

Genome mapping

We extracted genomic DNA using the DNeasy Blood and Tissue Kit (69504, QIAGEN) following the manufacturer's instructions. We pooled separately DNA samples of 19 *scl/scl* and 19 *scl/+* individuals in equimolar concentrations. We constructed short fragment size genomic DNA libraries for the two parents with the HiSeq Sequencing Kit TruSeq v4 and sequenced 125-bp paired-end reads using an Illumina HiSeq2000 instrument. We prepared genomic DNA libraries of 350-bp fragment size for the offspring pools with the TruSeq DNA PCR Free Kit and sequenced 151-bp paired-end reads with an Illumina HiSeqX instrument. We obtained 193 million to 316 million of paired-end reads per library and checked data quality and the absence of adapters with FASTQC (after adapter sequence removal with cutadapt v1.8). The remaining of the analyses for variant calling and the detection of candidate mutations were performed as previously described (*10*). The primers for the scl variant amplification and sequencing on complementary DNA (cDNA) and gDNA samples are provided in table S7.

Fibroblast isolation and transfection

Corn snake fibroblasts were isolated from embryonic tissue (*46*, *47*), cultured in minimum essential medium (M5650, Sigma) with 0.01% gentamicin (15750037, InvivoGen), 1% penicillin-streptomycin (15140122, Thermo Fisher Scientific), 1% amphotericin B (A2942, Sigma), 2 mM L-glutamine (G7513, Sigma), and 10% bovine calf serum (C8056, Sigma), and incubated at 30°C with 5% CO_2. gRNAs were designed with the Cas9 guide RNA design tool (Integrated DNA Technologies) and prepared with the Precision gRNA Synthesis Kit (A29377, Thermo Fisher Scientific). We transfected corn snake fibroblasts with a gRNA and TrueCut Cas9 Protein v2 (A36499, Thermo Fisher Scientific) mix (12.2 nM each) using the Lipofectamine CRISPRMAX Cas9 Transfection Reagent (CMAX00003, Thermo Fisher Scientific). We extracted fibroblast genomic DNA with the DNeasy Blood and Tissue Kit (69504, QIAGEN) and performed Sanger sequencing to verify the presence of mutations.

CRISPR-induced mutagenesis and verification

General anesthesia for the surgical procedure was induced by subcutaneous injection of a combination of dexmedetomidine (0.05 mg/kg) and midazolam (1 mg/kg). The animals were then intubated and maintained on intermittent positive pressure ventilation with 3

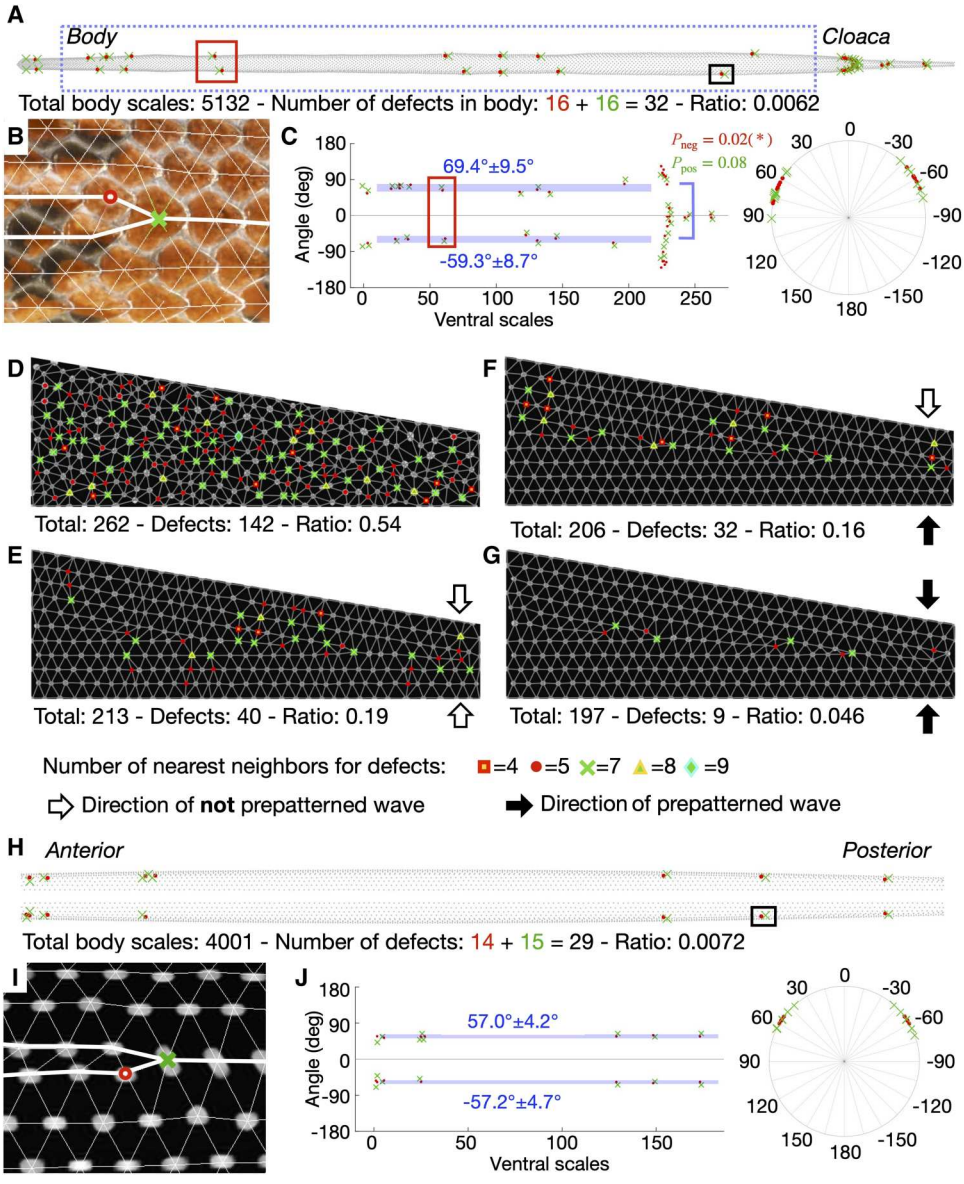

Fig. 8. Topological and statistical characterization of scale patterning defects. (**A**) Distribution of scale centers on the 3D surface geometry of an adult snake. Defects with five (red circles) and seven (green X) nearest neighbors are highlighted. (**B**) Detail [black frame in (A)] of a pair of defects resulting from the merge of two cephalocaudal rows into one. Nearest neighbor connectivity is indicated by white lines. (**C**) Angular distribution of defects on the body of the snake (left, as function of the nearest ventral scale; right, polar plot). The trunk region (excluding head, cloaca, and tail) is indicated in blue, and the average (± SD) of the angular distribution of defects is given for the right (positive) and left (negative) sides of the body. (A and C) The red rectangles highlight the last defect that results from the addition of a row of scales. Subsequent defects result from the merge of two rows. (**D** to **G**) Placode formation simulations on a planar domain: (D) in the absence of a traveling wave, (E) with two opposing traveling waves (white arrows), (F) with the interplacode distance of the initial row fixed (i.e., prepatterned, black arrow) for the lower wave, and (G) with both waves prepatterned. (**H**) Top view of the placode distribution produced by simulations with two prepatterned waves on an adult snake-like geometry. The third wave was not introduced in the simulations explaining the empty space along the dorsum. (**I**) Detail [black frame in (H)] of a pair of defects resulting from the merge of two rows into one. The black and white heatmap represents the value of *m* (mesenchymal cell density), with white spots of high values corresponding to placodes. (**J**) Angular distribution of defects resulting from the simulations (left, as function of the nearest ventral scale; right, polar plot).

to 7% sevoflurane in a mixture of oxygen and air. Ovaries were accessed through surgical incisions of the skin and body wall longitudinally between the ventral scales and the first row of lateral scales. Previtellogenic follicles were injected in situ using the Nanoject III Nanoliter Injector (Drummond Scientific) and pulled glass capillaries (3-000-203-G/X, Drummond Scientific). Two hundred nanoliters to 1.6 μl of a 5 μM ribonucleoprotein mix containing phenol red were injected in each pre-vitellogenic follicle depending on its size. Closure of the body wall and skin was performed with two layers of single interrupted surgical suture patterns with resorbable 5-0 Vicryl suture material. Reversal of the anesthesia was accomplished by intramuscular injection of flumazenil (0.1 mg/kg) and atipamezole (0.5 mg/kg). Analgesia was accomplished in a multimodal approach: (i) Preemptive analgesia was provided by subcutaneous

injection of meloxicam (0.2 mg/kg) at the induction of anesthesia, (ii) intraoperative analgesia was provided by dexmedetomidine and local infiltration of the skin incision site with lidocaine (4 mg/kg), and (iii) postoperative analgesia was provided by one daily subcutaneous injection with meloxicam (0.2 mg/kg) for 3 days. Antibiotic coverage was applied prophylactically (Ceftiofur CFA, 15 mg/kg, single subcutaneous injection).

Genomic DNA was extracted from the skin sheds of the offspring with the DNeasy Blood and Tissue Kit (69504, QIAGEN). The verification polymerase chain reaction (PCR) was done with the Q5 High-Fidelity DNA Polymerase (M0491S, Bioconcept). A-tailing was performed with the FastStart polymerase (12032902001, Sigma), and we subsequently cloned the amplified fragments of the scaleless offspring with the TA Cloning Kit Dual Promoter (K206001, Thermo Fisher Scientific). The vector of seven or eight clones per offspring was Sanger-sequenced. We performed primer walking to determine the deletion boundaries for individual 1 (primers in table S7).

WISH, immunostaining, and nuclear staining

We prepared species-specific riboprobes labeled with digoxigenin (table S7) and performed the in situ hybridizations on embryos fixed in paraformaldehyde as previously described (*48*). All scaleless embryos were genotyped and carried the 2-nt deletion in EDARADD. Embryos were imaged with a Keyence VHX-7000 digital microscope. Fluorescent in situ hybridizations were performed as described (*49*) with the modifications suggested by the manufacturer [HCR RNA-FISH (fluorescence in situ hybridization) protocol for whole-mount mouse embryos (*Mus musculus*), version 7, Molecular Instruments]. The EDA hybridization chain reaction (HCR) probe was hybridized to a hairpin labeled with Alexa Fluor 546, and the TROY HCR probe was hybridized to a hairpin labeled with Alexa Fluor 750 (Molecular Instruments). We cleared samples with iDISCO (*50*) and imaged them with an UltraMicroscope Blaze light sheet microscope (Miltenyi).

To visualize the somites, early-stage embryos were fixed in paraformaldehyde, permeabilized in PBSGST [0.2% gelatin, saponin (10 mg/ml), 0.5% Triton X-100, and 0.02% sodium azide in phosphate-buffered saline (PBS)], and nuclear-stained with TO-PRO-3 (T3605, Thermo Fisher Scientific). For immunostaining, the permeabilized embryos were incubated for 6 days with an anti-myosin monoclonal antibody (eBioscience, 14-5643-82) diluted at 1 μg/ml in PBSGST, washed with PBSGST, and incubated for four additional days with the secondary antibody (Goat anti-Mouse IgG, Alexa Fluor 546, Invitrogen A11030; 1:250 in PBSGST). They were all cleared with iDISCO (*50*) and imaged with an UltraMicroscope Blaze light sheet microscope (Miltenyi).

3D surface micro-geometry reconstruction

Body geometry as well as skin micro-geometry were obtained using R^2OBBIE (*35*), an automated image acquisition system, with a hybrid method of 3D reconstruction combining structure from motion and photometric stereo techniques (*35*). Dorsal and ventral scale detection was semi-automatized relying on the strong correlation between regions with high maximal principal curvature and interscale regions. Scale neighborhood was obtained by constructing local 2D Delaunay triangulations of projected scale boundary points (local projections of 3D positions in normal planes of patches). The angular coordinates of the defects were estimated by (i) taking a small segment of the snake body containing the defect, (ii) fitting a cylinder over the position of all the scales inside the segment, and (iii) evaluating the angular position of the defects on the corresponding cylindrical coordinates. The center of the ventral scale inside the segment was set to 180°, which fixes the angular origin. The statistical significance of the difference of the mean of absolute angle values was evaluated using a two-sample *t* test. Since positive and negative defects are highly correlated, we test them separately, although the averages and SDs are shown for the union of the two sets.

Reaction–diffusion–taxis model

We adapted the reaction–diffusion–taxis numerical simulation model proposed by Painter *et al.* (*36*) by introducing two modifications. First, the original model (*36*) introduced an exponential decay of m_0 in the direction of the wave propagation such that the density of m is always the same at the wavefront, i.e., $m_0 \sim \exp(-\alpha y)$. We remove this very fine-tuned assumption by making the growth rate of m proportional to the time derivative of the priming wave w while taking a uniform initial mesenchymal distribution $m_0 = 0.1$. Note that such a growth mechanism controlled by the temporal change of morphogen signaling has been demonstrated in other contexts (*51*–*53*). Second, we replaced the parametrization of the priming wave by a partial differential equation (PDE), which, on the plane, exactly admits the moving priming wave used in the original model as a stable solution. The key advantages of the PDE is that (i) it can be used more generally on arbitrary surfaces and (ii) it allows for the use of an arbitrary function $s_w(x,t)$ defining space-time positions of initial wave sources.

Numerical simulations were performed with a finite element method using piecewise linear shape functions for triangular meshes. Time discretization was done with the Euler method, where diffusion terms are evaluated backward (for increased numerical stability) and the other reaction and chemotactic terms are evaluated forward. Numerical simulations were performed with a custom Matlab script, with the use of the biconjugate gradient stabilized method "bicgstab()" as a linear solver.

Simulation parameters generating the result shown in Fig. 8 (D to G) and fig. S16 are as follows: $m_0 = 0.1$ (or 1.2 for "no wave"), $D_m = 0.01$, $D_f = 0.1$, $p_i = 2$, $K_1 = 1$, $K_2 = 3$, $K_3 = 5$, $\kappa_1 = 0.05$, $\kappa_2 = 0.025$, $\kappa_3 = \kappa_4 = 1$, $\alpha = 4$, $\delta = 1$, $r = \log(10)$, $\omega_1 = 1$, $\omega_2 = \omega_3 = 0.025$. When prepatterning is present, the interplacode distance in the initial row is $L = 3$. The geometry of the domain is a trapezoid with base length = $30L$, maximal height = $10L$, minimal height = $5L$. The domain is spatially discretized using ~209,500 triangles (mesh generated using MeshLab).

Simulation parameters generating the result shown in Fig. 8 (H to J) are as follows: $m_0 = 0.25$, $D_m = 0.01$, $D_f = 0.1$, $p_i = 2$, $K_1 = 2.5$, $K_2 = 7.5$, $K_3 = 12.5$, $\kappa_1 = 0.05$, $\kappa_2 = 0.025$, $\kappa_3 = 1$, $\kappa_4 = 0.4$, $\alpha = 4$, $\delta = 1$, $r = \log(7)$, $\omega_1 = 1$, $\omega_2 = \omega_3 = 0.03$. The top and bottom initial rows are prepatterned, and there is a quarter period shift between them. The domain is spatially discretized using ~1,405,000 triangles (mesh generated using MeshLab).

Simulation parameters generating the results shown in fig. S14 are as follows: $D_m = 0.01$, $D_f = 0.1$, $p_i = 2$, $K_1 = 1$, $K_2 = 3$, $K_3 = 5$, $\kappa_1 = 0.05$, $\kappa_2 = 0.025$, $\kappa_3 = \kappa_4 = 1$, $\alpha = 4$, $\delta = 1$, $\omega_1 = 1$, $\omega_2 = 0.2$, and $\omega_3 = 0.04$. For the original model (central panels in fig. S14C), we set $r_0 = 0.01$ and initial condition $m_0 = (2/3)\exp(-\alpha y)$, with α being the smaller root of $\alpha^2 - (\omega_3/D_m)\alpha + (r_0/D_m)$. For the modified model

(right panels), we set $r = \log(10)$ and initial condition $m_0 = 0.1$. These parameters were chosen so that the total amount of mesenchymal cells after the passing of the wave is similar in the two simulations.

Supplementary Materials

This PDF file includes:
Supplementary Text
Figs. S1 to S17
Tables S1 to S7
Legend for movie S1

Other Supplementary Material for this manuscript includes the following:
Movie S1

REFERENCES AND NOTES

1. J. B. Green, J. Sharpe, Positional information and reaction-diffusion: Two big ideas in developmental biology combine. *Development* **142**, 1203–1211 (2015).
2. S. Sick, S. Reinker, J. Timmer, T. Schlake, WNT and DKK determine hair follicle spacing through a reaction-diffusion mechanism. *Science* **314**, 1447–1450 (2006).
3. C. W. Cheng, B. Niu, M. Warren, L. H. Pevny, R. Lovell-badge, T. Hwa, K. S. E. Cheah, Predicting the spatiotemporal dynamics of hair follicle patterns in the developing mouse. *Proc. Natl. Acad. Sci. U.S.A.* **111**, 2596–2601 (2014).
4. S. I. Candille, C. D. V. Raamsdonk, C. Chen, S. Kuijper, Y. Chen-Tsai, A. Russ, F. Meijlink, G. S. Barsh, Dorsoventral patterning of the mouse coat by *Tbx15*. *PLOS Biol.* **2**, e3 (2004).
5. W. K. W. Ho, L. Freem, D. Zhao, K. J. Painter, T. E. Woolley, E. A. Gaffney, M. J. McGrew, A. Tzika, M. C. Milinkovitch, P. Schneider, A. Drusko, F. Matthäus, J. D. Glover, K. L. Wells, J. A. Johansson, M. G. Davey, H. M. Sang, M. Clinton, D. J. Headon, Feather arrays are patterned by interacting signalling and cell density waves. *PLOS Biol.* **17**, e3000132 (2019).
6. M. C. Milinkovitch, A. C. Tzika, Escaping the mouse trap: The selection of new Evo-Devo model species. *J. Exp. Zool. Part B* **308B**, 337–346 (2007).
7. A. C. Tzika, M. C. Milinkovitch, in *Evolving Pathways: Key Themes in Evolutionary DevelopmentalBiology*, A. Minelli, G. Fusco, Eds. (Cambridge Univ. Press, 2008), pp. 123–143.
8. A. Ullate-Agote, M. C. Milinkovitch, A. C. Tzika, The genome sequence of the corn snake (Pantherophis guttatus), a valuable resource for EvoDevo studies in squamates. *Int. J. Dev. Biol.* **58**, 881–888 (2014).
9. S. V. Saenko, S. Lamichhaney, A. M. Barrio, N. Rafati, L. Andersson, M. C. Milinkovitch, Amelanism in the corn snake is associated with the insertion of an LTR-retrotransposon in the *OCA2* gene. *Sci. Rep.* **5**, 17118 (2015).
10. A. Ullate-Agote, I. Burgelin, A. Debry, C. Langrez, F. Montange, R. Peraldi, J. Daraspe, H. Kaessmann, M. C. Milinkovitch, A. C. Tzika, Genome mapping of a LYST mutation in corn snakes indicates that vertebrate chromatophore vesicles are lysosome-related organelles. *Proc. Natl. Acad. Sci. U.S.A.* **117**, 26307–26317 (2020).
11. M. Toni, L. Alibardi, Soft epidermis of a scaleless snake lacks beta-keratin. *Eur. J. Histochem.* **51**, 145–151 (2007).
12. P. Licht, A. F. Bennett, A scaleless snake: Tests of the role of reptilian scales in water loss and heat transfer. *Copeia* **4**, 702–707 (1972).
13. A. F. Bennett, P. Licht, Evaporative water loss in scaleless snakes. *Comp. Biochem. Physiol.* **52**, 213–215 (1975).
14. N. Di-Poi, M. C. Milinkovitch, The anatomical placode in reptile scale morphogenesis indicates shared ancestry among skin appendages in amniotes. *Sci. Adv.* **2**, e1600708 (2016).
15. P. Jones, D. Binns, H. Y. Chang, M. Fraser, W. Li, C. McAnulla, H. McWilliam, J. Maslen, A. Mitchell, G. Nuka, S. Pesseat, A. F. Quinn, A. Sangrador-Vegas, M. Scheremetjew, S. Y. Yong, R. Lopez, S. Hunter, InterProScan 5: Genome-scale protein function classification. *Bioinformatics* **30**, 1236–1240 (2014).
16. A. Morlon, A. Munnich, A. Smahi, TAB2, TRAF6 and TAK1 are involved in NF-kappaB activation induced by the TNF-receptor, Edar and its adaptator Edaradd. *Hum. Mol. Genet.* **14**, 3751–3757 (2005).
17. A. Sadier, L. Viriot, S. Pantalacci, V. Laudet, The ectodysplasin pathway: From diseases to adaptations. *Trends Genet.* **30**, 24–31 (2014).
18. J. Reyes-Reali, M. I. Mendoza-Ramos, E. Garrido-Guerrero, C. F. Méndez-Catalá, A. R. Méndez-Cruz, G. Pozo-Molina, Hypohidrotic ectodermal dysplasia: Clinical and molecular review. *Int. J. Dermatol.* **57**, 965–972 (2018).
19. B. Beutler, colleagues, Record for achtung. MUTAGENETIX (TM) - Center for the Genetics of Host Defense, UT Southwestern, Dallas, TX (2016).
20. T. Wang, C. H. Bu, S. Hildebrand, G. Jia, O. M. Siggs, S. Lyon, D. Pratt, L. Scott, J. Russell, S. Ludwig, A. R. Murray, E. M. Y. Moresco, B. Beutler, Probability of phenotypically detectable protein damage by ENU-induced mutations in the Mutagenetix database. *Nat. Commun.* **9**, 441 (2018).
21. N. Chassaing, C. Cluzeau, E. Bal, P. Guigue, M. C. Vincent, G. Viot, D. Ginisty, A. Munnich, A. Smahi, P. Calvas, Mutations in EDARADD account for a small proportion of hypohidrotic ectodermal dysplasia cases. *Br. J. Dermatol.* **162**, 1044–1048 (2010).
22. S. Kondo, Y. Kuwahara, M. Kondo, K. Naruse, H. Mitani, Y. Wakamatsu, K. Ozato, S. Asakawa, N. Shimizu, A. Shima, The medaka rs-3 locus required for scale development encodes ectodysplasin-A receptor. *Curr. Biol.* **11**, 1202–1206 (2001).
23. M. P. Harris, N. Rohner, H. Schwarz, S. Perathoner, P. Konstantinidis, C. Nüsslein-Volhard, Zebrafish eda and edar mutants reveal conserved and ancestral roles of ectodysplasin signaling in vertebrates. *PLOS Genet.* **4**, e1000206 (2008).
24. A. M. Rasys, S. Park, R. E. Ball, A. J. Alcala, J. D. Lauderdale, D. B. Menke, CRISPR-Cas9 gene editing in lizards through microinjection of unfertilized oocytes. *Cell Rep.* **28**, 2288–2292.e3 (2019).
25. H. Ma, N. Marti-Gutierrez, S. W. Park, J. Wu, Y. Lee, K. Suzuki, A. Koski, D. Ji, T. Hayama, R. Ahmed, H. Darby, C. van Dyken, Y. Li, E. Kang, A. R. Park, D. Kim, S. T. Kim, J. Gong, Y. Gu, X. Xu, D. Battaglia, S. A. Krieg, D. M. Lee, D. H. Wu, D. P. Wolf, S. B. Heitner, J. C. I. Belmonte, P. Amato, J. S. Kim, S. Kaul, S. Mitalipov, Correction of a pathogenic gene mutation in human embryos. *Nature* **548**, 413–419 (2017).
26. M. C. Milinkovitch, L. Manukyan, A. Debry, N. di-Poï, S. Martin, D. Singh, D. Lambert, M. Zwicker, Crocodile head scales are not developmental units but emerge from physical cracking. *Science* **339**, 78–81 (2013).
27. J. M. Musser, G. P. Wagner, R. O. Prum, Nuclear β-catenin localization supports homology of feathers, avian scutate scales, and alligator scales in early development. *Evol. Dev.* **17**, 185–194 (2015).
28. K. L. Wells, Y. Hadad, D. Ben-Avraham, J. Hillel, A. Cahaner, D. J. Headon, Genome-wide SNP scan of pooled DNA reveals nonsense mutation in FGF20 in the scaleless line of featherless chickens. *BMC Genomics* **13**, 257 (2012).
29. S. H. Huh, K. Närhi, P. H. Lindfors, O. Häärä, L. Yang, D. M. Ornitz, M. L. Mikkola, Fgf20 governs formation of primary and secondary dermal condensations in developing hair follicles. *Genes Dev.* **27**, 450–458 (2013).
30. L. Houghton, C. Lindon, B. A. Morgan, The ectodysplasin pathway in feather tract development. *Development* **132**, 863–872 (2005).
31. J. Pispa, M. Pummila, P. A. Barker, I. Thesleff, M. L. Mikkola, Edar and Troy signalling pathways act redundantly to regulate initiation of hair follicle development. *Hum. Mol. Genet.* **17**, 3380–3391 (2008).
32. C.-Y. Cui, M. Kunisada, Y. Piao, V. Childress, M. S. H. Ko, D. Schlessinger, Dkk4 and Eda regulate distinctive developmental mechanisms for subtypes of mouse hair. *J. Invest. Dermatol.* **5**, –S102 (2010).
33. C. F. Drew, C. M. Lin, T. X. Jiang, G. Blunt, C. Mou, C. M. Chuong, D. J. Headon, The Edar subfamily in feather placode formation. *Dev. Biol.* **305**, 232–245 (2007).
34. L. Houghton, C. M. Lindon, A. Freeman, B. A. Morgan, Abortive placode formation in the feather tract of the scaleless chicken embryo. *Dev. Dyn.* **236**, 3020–3030 (2007).
35. A. F. Martins, M. Bessant, L. Manukyan, M. C. Milinkovitch, R(2)OBBIE-3D, a fast robotic high-resolution system for quantitative phenotyping of surface geometry and colour-texture. *PLOS ONE* **10**, e0126740 (2015).
36. K. J. Painter, W. Ho, D. J. Headon, A chemotaxis model of feather primordia pattern formation during avian development. *J. Theor. Biol.* **437**, 225–238 (2018).
37. A. M. Turing, The chemical basis of morphogenesis. *Bull. Math. Biol.* **52**, 153–197 (1953).
38. A. Gierer, H. Meinhardt, A theory of biological pattern formation. *Kybernetik* **12**, 30–39 (1972).
39. C. Mou, F. Pitel, D. Gourichon, F. Vignoles, A. Tzika, P. Tato, L. Yu, D. W. Burt, B. Bed'hom, M. Tixier-Boichard, K. J. Painter, D. J. Headon, Cryptic patterning of avian skin confers a developmental facility for loss of neck feathering. *PLOS Biol.* **9**, e1001028 (2011).
40. K. J. Painter, G. S. Hunt, K. L. Wells, J. A. Johansson, D. J. Headon, Towards an integrated experimental-theoretical approach for assessing the mechanistic basis of hair and feather morphogenesis. *Interface Focus* **2**, 433–450 (2012).
41. A. J. Aman, M. Kim, L. M. Saunders, D. M. Parichy, Thyroid hormone regulates abrupt skin morphogenesis during zebrafish postembryonic development. *Dev. Biol.* **477**, 205–218 (2021).
42. G. Cherepanov, Y. Malashichev, I. Danilov, Supernumerary scutes verify a segment-dependent model of the horny shell development in turtles. *J. Anat.* **235**, 836–846 (2019).
43. J. E. Moustakas-Verho, R. Zimm, J. Cebra-Thomas, N. K. Lempiäinen, A. Kallonen, K. L. Mitchell, K. Hämäläinen, I. Salazar-Ciudad, J. Jernvall, S. F. Gilbert, The origin and loss of periodic patterning in the turtle shell. *Development* **141**, 3033–3039 (2014).

44. R. Zimm, D. Oberdick, A. Gnetneva, P. Schneider, J. Cebra-Thomas, J. E. Moustakas-Verho, Turing's turtles all the way down: A conserved role of EDAR in the carapacial ridge suggests a deep homology of prepatterns across ectodermal appendages. *Anat. Rec.* **306**, 1201–1213 (2023).
45. J. G. Capano, Reaction forces and Rib function during locomotion in snakes. *Integr. Comp. Biol.* **60**, 215–231 (2020).
46. L. F. Andrade, P. Villegas, O. J. Fletcher, Vaccination of day-old broilers against infectious bronchitis: Effect of vaccine strain and route of administration. *Avian Dis.* **27**, 178–187 (1983).
47. R. Hernandez, D. T. Brown, Growth and maintenance of chick embryo fibroblasts (CEF). *Curr. Protoc. Microbiol.* **4**, 4I (2010).
48. R. D. Riddle, R. L. Johnson, E. Laufer, C. Tabin, Sonic hedgehog mediates the polarizing activity of the ZPA. *Cell* **75**, 1401–1416 (1993).
49. H. M. T. Choi, M. Schwarzkopf, M. E. Fornace, A. Acharya, G. Artavanis, J. Stegmaier, A. Cunha, N. A. Pierce, Third-generation in situ hybridization chain reaction: Multiplexed, quantitative, sensitive, versatile, robust. *Development* **145**, (2018).
50. N. Renier, Z. Wu, D. J. Simon, J. Yang, P. Ariel, M. Tessier-Lavigne, iDISCO: A simple, rapid method to immunolabel large tissue samples for volume imaging. *Cell* **159**, 896–910 (2014).
51. O. Wartlick, F. Julicher, M. Gonzalez-Gaitan, Growth control by a moving morphogen gradient during Drosophila eye development. *Development* **141**, 1884–1893 (2014).
52. O. Wartlick, P. Mumcu, A. Kicheva, T. Bittig, C. Seum, F. Jülicher, M. González-Gaitán, Dynamics of Dpp signaling and proliferation control. *Science* **331**, 1154–1159 (2011).
53. R. Mateus, L. Holtzer, C. Seum, Z. Hadjivasiliou, M. Dubois, F. Jülicher, M. Gonzalez-Gaitan, BMP signaling gradient scaling in the zebrafish pectoral fin. *Cell Rep.* **30**, 4292–4302.e7 (2020).

Acknowledgments: We thank the following collaborators for technical assistance (in alphabetical order): I. Burgelin, A. Debry, V. Haechler, C. Langrez, and F. Montange. Electron microscopy imaging was performed at the Bioimaging Center, University of Geneva. Head CT scans were performed at the "Plateforme d'Imagerie Préclinique du Petit Animal (PIPPA)," University of Geneva. Full-body CT scans were performed at the "Centre universitaire romand de médecine légale" with the help of R. Soto. **Funding:** This work was supported by the Swiss National Science Foundation (31003A_179431 to M.C.M. and 310030_204466 to A.C.T.), the Georges et Antoine Claraz Foundation (to M.C.M. and A.C.T.), the iGE3 PhD salary award (to A.U.-A.), and the Sara Borrell grant (CD22/00027) from the Instituto Carlos III and NextGenerationEU (to A.U.-A.). **Author contributions:** Conceptualization: A.C.T. Data curation: A.C.T. and A.U.-A. Funding acquisition: A.C.T. and M.C.M. Investigation: A.C.T., A.U.-A., S.Z., and M.K. Methodology: A.C.T., A.U.-A., S.Z., M.K., and M.C.M. Project administration: A.C.T. Software: A.U.-A. and S.Z. Supervision: A.C.T. and M.C.M. Validation: A.C.T. Visualization: A.C.T., A.U.-A., and S.Z. Writing—original draft: A.C.T., A.U.-A., and S.Z. Writing—review and editing: A.C.T., A.U.-A., S.Z., M.K., and M.C.M. **Competing interests:** The authors declare that they have no competing interests. **Data and materials availability:** All data needed to evaluate the conclusions in the paper are present in the paper and/or the Supplementary Materials. Sequencing data are available on NCBI (https://www.ncbi.nlm.nih.gov/, accession number: GCA_001185365.2).

Submitted 18 November 2022
Accepted 12 May 2023
Published 14 June 2023
10.1126/sciadv.adf8834